

# Impurity-induced topological phase transitions in $Cd_3As_2$ and $Na_3Bi$ Dirac semimetals

A. Rancati,<sup>1,3</sup> N. Pournaghavi,<sup>2</sup> M. F. Islam,<sup>2</sup> A. Debernardi,<sup>3</sup> and C.M. Canali<sup>2</sup>

<sup>1</sup>*Univ Insubria, Dipartimento Sci & Alta Tecnol, Via Valleggio 11, I-22100 Como, Italy*

<sup>2</sup>*Linnaeus University, Department of Physics and Electrical Engineering, 392 31 Kalmar, Sweden*

<sup>3</sup>*CNR-IMM, sede Agrate Brianza, via Olivetti 2, I-20864 Agrate Brianza, Italy*

(Dated: November 12, 2020)

Using first-principles density functional theory calculations, combined with a topological analysis, we have investigated the electronic properties of  $Cd_3As_2$  and  $Na_3Bi$  Dirac topological semimetals doped with non-magnetic and magnetic impurities. Our systematic analysis shows that the selective breaking of the inversion, rotational and time-reversal symmetry, controlled by specific choices of the impurity doping, induces phase transitions from the original Dirac semimetal to a variety of topological phases such as, topological insulator, trivial semimetal, non-magnetic and magnetic Weyl semimetal, and Chern insulator. The Dirac semimetal phase can exist only if the rotational symmetry  $C_n$  with  $n > 2$  is maintained. One particularly interesting phase emerging in doped  $Cd_3As_2$  is a coexisting Dirac-Weyl phase, which occurs when only inversion symmetry is broken while time-reversal symmetry and rotational symmetry are both preserved. To further characterize the low-energy excitations of this phase, we have complemented our density functional results with a continuum four-band  $k \cdot p$  model, which indeed displays nodal points of both Dirac and Weyl type. The coexisting phase appears as a transition point between two topologically distinct Dirac phases, but may also survive in a small region of parameter space controlled by external strain.

## I. INTRODUCTION

Topological Dirac materials are a class of advanced materials characterized by electronic excitations with a linear dispersion about some nodal points close to the Fermi level[1–5]. Since the theoretical prediction[6, 7] and the subsequent experimental discovery[8] of time-reversal-invariant three-dimensional (3D) topological insulators (TIs), displaying two-dimensional (2D) surface states with a spin-momentum-locked linear dispersion around nodal Dirac points (DPs), there has been an intense search for materials that host 3D Dirac fermions with linear dispersion in all three momentum directions. By using theoretical models, the existence of such gapless nodes in 3D bulk system was predicted by Murakami as a transition point between the quantum spin Hall and the insulator phases[9]. In systems possessing both inversion symmetry (IS) and time-reversal symmetry (TRS), this transition results in four-fold degenerate 3D Dirac nodes. For systems in which IS or TRS is broken, the gapless nodes are two-fold degenerate nodes known as Weyl points (WPs). Since the nodal points occur at around the Fermi energy, these materials are known as Dirac semimetals (DSMs) and Weyl semimetals (WSMs), respectively. Materials hosting topologically protected Dirac or Weyl fermions as elementary excitations have the potential to revolutionize low-energy high-performance spin-electronics. For a detailed review of the properties of topological semimetals, see Ref. 10.

The search for stable 3D DSMs in realistic systems experienced a breakthrough with the studies of  $Na_3Bi$  and  $Cd_3As_2$  compounds. Using density functional theory (DFT) methods, it was shown theoretically that a pair of stable 3D DPs, protected by the rotational symmetry of the space groups of these crystals, exists on the  $k_z$  axis[11, 12]. Eventually, by employing angle-resolved

photoemission spectroscopy, these Dirac nodes were observed in  $Na_3Bi$ [13, 14] and  $Cd_3As_2$ [15, 16] semimetals. Since the realization of WSM requires breaking of IS or TRS or both, it has been predicted theoretically that pyrochlore iridate materials[17], topological multilayer structures[17] and TaAs class of systems[18–20] can host Weyl nodes. Shortly after these predictions, the existence of WSMs was verified in experiments with TaAs[21] and TaP[22].

The degeneracy associated with WP does not rely on any particular symmetry other than the translation symmetry of the crystal lattice. Each WP is characterized by a topological charge of a definite (positive or negative) chirality, corresponding to a bulk Chern number. This makes the properties of the bulk electronic bandstructure topologically robust against external perturbations. Moreover, as a result of the bulk-edge correspondence, the non-trivial bulk topology of a WSM gives rise to robust Fermi arc surface states[17, 18, 22–24]. Weyl fermions in WSMs are predicted to possess unusual transport phenomena[25]. For example, in the bulk they can give rise to negative magnetoresistance, anomalous Hall effect, non-local transport and local non-conservation of ordinary current[26–29]. Weyl Fermi arc surface states on the other hand are predicted to show novel quantum oscillations in magnetotransport and quantum interference effects in tunnelling spectroscopy[30–32]. Similar to WSMs, double Fermi arc surface states are also observed in DSMs[33] but they may not have any topological protection in general[34, 35].

Apart from naturally occurring WSM materials, such as the TaAs class, it is interesting and important to investigate materials that can become WSMs as a result of topological phase transitions induced by external perturbations. For example, phase transitions from DSMs to other topological phases, included WSMs, were dis-

cussed by Yang *et al.*, using theoretical models[36]. The simplest way to turn a DSM into a WSM is to apply an external magnetic field, which breaks TRS. In  $Cd_3As_2$ , a magnetic field-driven splitting of Landau levels and a nontrivial Berry phase were detected[37], which are consistent with the Weyl phase.

On the other hand, considerably less investigated are the topological phase transitions induced by doping DSMs. Different types of impurities and the ways in which they are incorporated in pristine DSM materials, can selectively break the symmetries that are required for the stability of the Dirac nodes in a DSM. This leads to a variety of phase transitions to both topologically trivial or non-trivial phases. First-principles studies[38] of  $Na_3Bi$  and  $Cd_3As_2$  DSMs alloyed with Sb and P, carried out within coherent potential approximation (CPA) where the crystal symmetries are preserved, show that these materials remain in the DSM phase up to 50% concentration before making a transition to a trivial insulator[38]. More recently, the effect of magnetic impurities in DSMs has been studied theoretically within a model Hamiltonian approach, showing that the breaking of TRS by magnetic impurity potential splits a Dirac node into two Weyl nodes[39].

In this work, using DFT methods, we have systematically investigated the effect of nonmagnetic zinc (Zn) and magnetic manganese (Mn) impurities in the prototypical  $Cd_3As_2$  and  $Na_3Bi$  DSMs. In particular, we have carefully introduced impurities to break selectively different symmetries, and have analyzed the consequences of terms that break individual or multiple symmetries on the topological properties. We have also investigated the combined effect of doping and strain on the topological properties. Our work shows that a DSM makes transitions to a WSM, a topological insulator or an ordinary insulator phase, depending on which symmetry is broken. Importantly, we find that in doped  $Cd_3As_2$  where IS is broken by nonmagnetic impurities while TRS and rotational symmetry are preserved, modified DSM and WSM phases can even coexist at special points of the parameter space, which can be reached by applying an external strain. This occurrence bears some similarities to the mixed phase recently found theoretically in polar hexagonal  $ABC$  Crystal SrHgPb[40]. When TRS or both TRS and IS are broken, the system makes a transition to a magnetic Weyl phase.

The paper is organized as follows. In Sec. II we describe the details of the computational approach, which include the DFT methods and the topological analysis based on the calculations of different topological invariants carried in atomistic tight-binding models extracted from DFT. In Sec. III we present the results for pure  $Cd_3As_2$  and the consequences of different symmetry breaking, and in Sec. IV we have discussed our calculations of antimony (Sb) doped  $Na_3Bi$  DSM. Finally, in Sec.V we present the conclusions and outlook.

## II. COMPUTATIONAL DETAILS

We have used three different computational tools to study the electronic and the topological properties of  $Cd_3As_2$  and  $Na_3Bi$  DSMs.

*DFT* – To perform electronic structure calculations, we have first relaxed the crystal structure for both the cell parameters and the atomic positions using the Quantum Espresso ab-initio code[41]. The final relaxed structure is then used to study electronic properties in the presence of spin-orbit coupling, by employing the full-potential all-electron linearized augmented plane-waves method as implemented in WIEN2K ab-initio code[42]. The Perdew-Burke-Ernzerhof generalized gradient approximation (PBE-GGA) is used for the exchange correlation functional[43]. For a few calculations (Mn doping) we have employed the Vienna Ab Initio Simulation Package (VASP)[44, 45]. We have checked a few benchmark cases with both Wien2k and VASP, finding that the two DFT codes give consistent results.

The crystal structure of  $Cd_3As_2$  at ambient conditions has the tetragonal symmetry  $D_{4h}^{15}$  ( $P_{42}/nmc$ ), with a 40-atom unit cell[46]. The symmetries that play a crucial role in the electronic properties of this crystal are TRS, IS, two mirror planes ( $M_{xz}$  and  $M_{yz}$ ), and a nonsymmorphic screw symmetry  $S_{4z}$  (consisting of a 4-fold rotation about the z-axis followed by a half lattice translation along the z-axis). We will see later that this screw axis is essential for the stability of the DPs. Note that apart from these symmetries, the point group of the crystal also contains dihedral mirror planes and  $C_2$  rotation axes.

We have constructed the cell using the experimental lattice constants and have relaxed both the cell parameters and the atomic positions until the forces are less than 1 mRy/au and the stress on the cell is less than 0.5 Kbar. The energy convergence was set to  $10^{-3}$  mRy. This calculation is performed using Quantum Espresso with the cutoff energies  $E_{wfc} = 80$  Ry for the wave function and  $E_\rho = 600$  Ry for the charge density and potential; a uniform Monkhorst-Pack mesh of  $7 \times 7 \times 5$  k-points has been used. The relaxation increases the cell parameters from ( $a=b=16.89$ ,  $c=23.96$  bohr) to ( $a=b=17.27$ ,  $c=24.27$  bohr). The atomic positions also change after relaxation, but not very significantly. This relaxed structure is the basis of the remaining calculations performed in this work.

The topological phase transitions are studied by introducing different realizations of substitutional Zn or Mn impurities at Cd sites in order to break different symmetries of the system. We have chosen Zn and Mn as substitutional impurities for Cd because these elements have the same valence states of Cd (two electrons in the s states) and atomic radii close to the one of Cd, which minimizes the stress induced by alloying. Note that Zn and Mn are usually substitutional impurities of Cd in II-VI compounds, and both alloys,  $Cd_{3-x}Zn_xAs_2$  and  $Cd_{3-x}Mn_xAs_2$  have been synthesized [47–49].

Before analyzing different cases, a few comments on the how impurity doping is introduced in the crystal in the first-principles calculations are in order. Although for a given impurity concentration several structural configurations are in principle possible, the constraint of breaking one particular symmetry while preserving the others reduces significantly the number of different realizations that are actually allowed. Even when we have more than one disordered realization for breaking a given symmetry, those configurations themselves are related by the remaining symmetries of the crystal, and therefore they are not expected to provide significantly different results.

However, in the case where both inversion and rotational symmetries are broken by substituting only one Cd by a Zn atom (this will be the case leading to a Weyl phase), there exist multiple, genuinely-different, doping configurations that should be addressed. Since these calculations are very time consuming, we have limited ourselves to consider only two different disordered configurations. Typically we find that, except for a small difference in the bandstructure, the topological properties are the same for both configurations.

The different types of chemical doping and the different impurity concentrations that we have considered in this work are the following:

1. 4 Zn atoms in the 40-atoms unit cell, with 24 Cd atoms ( $\sim 17\%$  of dopants), placed in order to maintain inversion symmetry (IS) while breaking the  $S_{4z}$ . We have also considered 2 Zn atoms ( $\sim 9\%$  of dopants) to preserve IS and  $C_2$  while breaking the  $S_{4z}$ .
2. 1 Zn atom ( $\sim 4\%$  of dopants), in order to break both IS and  $S_{4z}$ .
3. 12 Zn atoms (50% of dopants), which simulates  $\delta$  doping (dopants placed on planes perpendicular to the rotation axis), in order to break IS while preserving  $S_{4z}$  (see Fig 1a).
4. 2 Mn atom ( $\sim 8\%$  doping), in order to break TRS and 1Mn atom to break both IS and TRS.

After relaxing the system for each of these impurity cases, we have investigated their projected band structure using the Wien2k code.

*Wannier90* – For the topological studies of this system, we have constructed a real-space tight-binding (TB) Hamiltonian in the basis of the Wannier states. The Wannier90 code[50] is used to construct Maximally Localized Wannier Functions (MLWFs) from the Kohn-Sham orbitals obtained from the Wien2k calculations. Since the DFT calculations show that the states near the Fermi level are predominantly  $5s$  of Cd,  $4s$  and  $4p$  of As, and  $4s$  of Zn atoms (more detailed discussion is in section III), we initially projected the Bloch states on these orbitals. Furthermore, taking into account the spin-orbit coupling, we have considered the Wannier functions as spinors, namely two component states, and therefore a

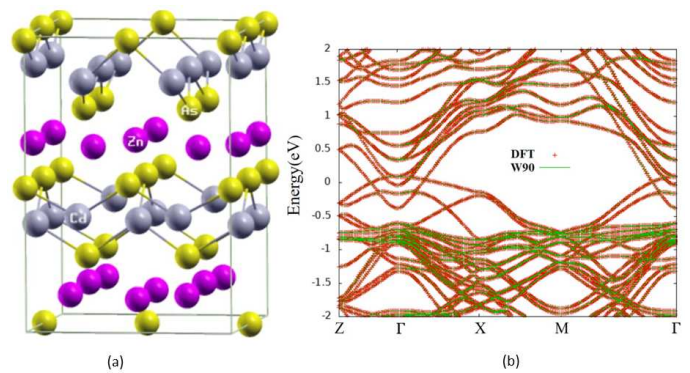


FIG. 1. a) Relaxed structure of  $Cd_3As_2$  doped with 12 Zn atoms to break IS while preserving  $S_{4z}$ . This type of doping is known as  $\delta$ -doping and is easily realizable experimentally. b) Comparison of the Zn-doped  $Cd_3As_2$  bandstructure obtained from DFT and that from the real-space tight-binding Hamiltonian in the maximally localized Wannier basis. The good agreement between these two methods demonstrates that the Wannierization procedure is satisfactory.

total of 176 Wannier functions have been chosen. In the case of Mn magnetic impurities, we have taken into account also their  $3d$  orbitals, which increased the total Wannier functions up to 186.

The accuracy of the calculation of the topological properties relies on the accuracy of MLWFs. We have used two criteria for acceptable accuracy: (i) the spread of the Wannier functions should be smaller than the smallest lattice constant; (ii) the bands calculated from the Wannier Hamiltonian should be a good match with the DFT bands. Furthermore, to reduce the numerical error during the Wannierization, we have also implemented disentanglement, a procedure to project out the contribution of the relevant from unwanted bands[51]. Fig 1b shows the DFT and Wannier90 bands for the impurity case 3 mentioned above. A good match reflects the fact that satisfactory MLWFs have been achieved.

*WannierTools* – The real space Hamiltonian obtained from Wannier90 code is then used in WannierTools[52] to study different topological properties of the system. The code is used to search for the nodes in the Brillouin zone (BZ), and to calculate different topological indices such as  $Z_2$ , Chern number etc., which helps to identify different topological phases. In WannierTools, the  $Z_2$  and the Chern number are calculated using the Wannier Charge Center (WCC) method[53]. According to this method, a hybrid Wannier function is constructed for each band by integrating out one component of  $\mathbf{k}$  vector, say  $k_z$ . The WCC of band  $n$  is then the expectation value of  $r_z(k_x, k_y)$  in this hybrid Wannier function. The evolution of the WCCs along a k-path in a given plane, say the  $k_x - k_y$  plane, of the BZ can be used to calculate the topological properties of the plane. For details see Ref. 53.

A similar strategy has been also employed to study the electronic and topological properties of  $Na_3Bi$ . The

unit cell of hexagonal  $Na_3Bi$  crystal contains eight atoms (two Bi and six Na atoms). It turns out that the crystal structure is such that in order to break one specific symmetry without breaking the remaining ones (for example, breaking the screw symmetry while maintaining the IS) requires considerably large supercells. A large supercell requires many Wannier functions for achieving an acceptable Wannierization procedure, and it also introduces many bands in the first BZ due to band folding, which makes it difficult to study the topological properties reliably. For this reason, we have considered only the case with broken IS.

### III. TOPOLOGICAL PHASE TRANSITIONS IN DOPED $Cd_3As_2$ DSM

The presence of IS and TRS in pure  $Cd_3As_2$  leads to the double degeneracy of each band. When band inversion between the conduction band (primarily consisting of Cd  $s$  states) and the valence band (primarily consisting of As  $p$  states) occurs, as shown in Fig 2a, two Dirac nodes appear symmetrically around the  $\Gamma$ -point on the Z- $\Gamma$  axis at  $(0, 0, \pm 0.081)(1/\text{\AA})$ , consistent with previous works[13, 54–56]. The two DPs lie at  $-0.008$  eV, slightly below the Fermi energy. The system can be further characterized by the  $Z_2$  invariant of the six time-reversal-invariant planes (TRIPs). Since the Dirac nodes are on the  $k_z$  axis, only  $k_z=0$  and  $k_x, k_y, k_z = \pi$  planes are gapped. Our calculations show that  $Z_2=1$  only for the  $k_z = 0$ -plane, implying that the associated gap is non-trivial. We have further verified the existence of *double Fermi arcs* surface states, as shown in the inset of Fig 2a. These results serve as a benchmark for the calculations of the doped cases described below.

#### A. Non-magnetic impurities in $Cd_3As_2$

In this section we study the effect of doping on the electronic and topological properties of  $Cd_3As_2$ , when IS,  $C_2$  rotational symmetries, and  $S_{4z}$  screw symmetry, are selectively broken, while TRS is preserved. This is achieved by introducing substitutional non-magnetic Zn impurities at the Cd sites. Here we discuss three different impurity realizations and their consequences on the topological properties.

##### 1. Broken $S_{4z}$ screw symmetry: transition to $Z_2$ semimetal and insulator phases

In order to break the  $S_{4z}$  screw symmetry while preserving IS (and TRS), we have substituted four Cd atoms by 4 Zn atoms. Since both TRS and IS are still present, all bands are two-fold degenerate. However, by breaking the screw symmetry we also break other symmetries

such as mirror planes and, consequently, the space group reduces to P-1, which contains only the IS. At a general point on the  $k_z$  axis, the point group is  $C_1$ , which contains only the unit operator. Therefore, both the conduction and valence band states belong to the  $A_1$  irreducible representation of this point group, and they are allowed to mix when they approach each other. Consequently, the Z- $\Gamma$  path becomes gapped, as shown in Fig 2b. Our DFT calculations show that the smallest gap is of the order of 40 meV at around  $(0, 0, \pm 0.095)(1/\text{\AA})$ , which is slightly away from the DPs of the pure  $Cd_3As_2$ .

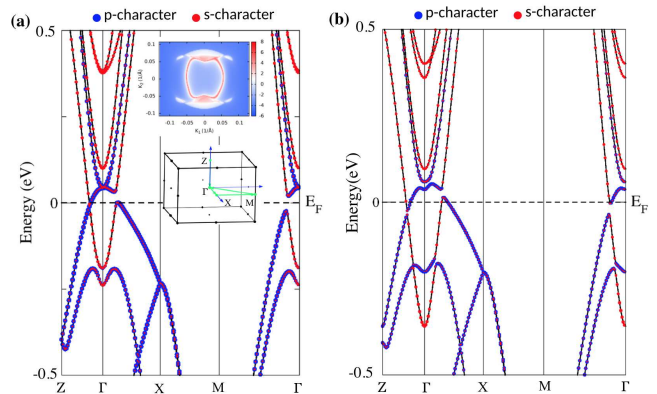


FIG. 2. (a) The projected bandstructure of  $Cd_3As_2$ . The presence of Cd  $s$  states (red) below the Fermi level and As  $p$  states (blue) above the Fermi level indicates that bands are inverted around the  $\Gamma$ -point, leading to nontrivial topology. The inset shows the existence of *double Fermi arcs* surface states. (b) The projected bandstructure of Zn doped  $Cd_3As_2$  with broken  $S_{4z}$  screw symmetry. Band inversion is still preserved as in case of (a), signaling a non-trivial topology, but a gap opens up at the DP.

The projected orbital states in Fig 2b shows that the valence band is predominantly of As  $p$  character (blue) whereas the conduction band is predominantly of Cd  $s$  and Zn  $s$  character (red). It is also evident that around the  $\Gamma$ -point bands are inverted as there is a considerable presence of  $s$  states just below the Fermi level and  $p$  states above the Fermi level, which gives rise to the non-trivial topology.

We note from the bandstructure that this system is not a proper insulator, but rather a semimetal, since the Fermi level crosses both the conduction and valence bands, creating an electron pocket on Z- $\Gamma$  path and a hole pocket on  $\Gamma$ -X path, respectively. However, since the valence band has a finite *direct* bandgap everywhere in the BZ, it can be topologically classified in the same way as it is done for bismuth and antimony semimetals[1]. Therefore, we have calculated the  $Z_2$  indices for all the six TRIPs ( $k_x = 0, \pi; k_y = 0, \pi; k_z = 0, \pi$ ). We find that  $Z_2=1$  for the  $k_x, k_y, k_z = 0$  planes and zero for all other planes. The topological index of the system is then  $\nu=(1;0,0,0)$ , which is the same index of a strong 3D topological insulator. Although this system is considered as a semimetal due to the presence of a few states at the Fermi

level, the non-trivial  $Z_2$  topology suggests the existence of non-trivial surface states for this system.

To further confirm that  $S_{4z}$  is necessary for the stability of the Dirac nodes, we have performed an additional calculation where both IS and  $C_2$  are preserved but  $S_{4z}$  is broken (space group  $P2_1/m$ ), which is realized by substituting two Cd by two Zn atoms. In this case, the Fermi level is fully gapped everywhere in the BZ, with the smallest gap being of the order of 30 meV at the original location of the DPs. The bandstructure is similar to that of Fig 2b, except that the bands do not cross the Fermi level. The topological analysis shows that this system is also a strong TI with  $\nu=(1;0,0,0)$ .

These calculations clearly demonstrate the importance of the rotational  $S_{4z}$  screw symmetry for the stability of the DPs in the  $Cd_3As_2$ , consistent with the stability criteria discussed in [36]. They also show how breaking this symmetry can cause a transition to a topologically distinct phase.

## 2. Broken IS and $S_{4z}$ symmetry: transition to a Weyl phase

In this section we discuss the effect of breaking both IS and  $S_{4z}$  screw symmetry. This can be achieved simply by replacing one Cd atom by one Zn atom in the unit cell. As a result of this impurity configuration, the space group of the crystal changes to Pm space, which contains only a reflection plane. Since the IS is absent in this space group, the bands are no longer doubly degenerate, except at the TRIMs. Consequently, Dirac nodes cannot form at any high symmetry line. Indeed, a gap of 30 meV opens up at the location of the DP of the pure system, as shown in Fig 3a. However, this opens up the possibility that each Dirac node may split into two Weyl nodes. To search for the Weyl nodes, we have con-

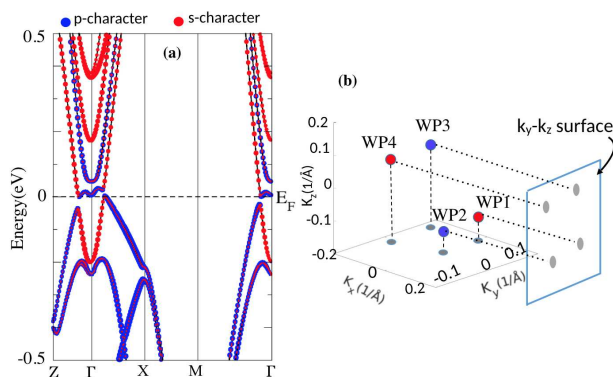


FIG. 3. (a) The bandstructure of  $Cd_3As_2$  with broken IS and  $S_{4z}$  screw symmetry. As  $p$  and Cd  $s$  states are highlighted with blue and red, respectively. (b) Each Dirac node splits into two Weyl nodes of opposite chirality. The red (blue) dots represent Weyl nodes of +1 (-1) chirality. The projection of the Weyl nodes on the  $k_x - k_y$  and  $k_x - k_z$  planes is also shown.

structed the real-space TB Hamiltonian in the WF basis as described in section II. We have then searched for the nodes between the highest occupied and the lowest unoccupied bands in the entire BZ using WannierTools. We found four nodes in the BZ at  $k$ -values  $(0.067, \pm 0.025, -0.042)(1/\text{\AA})$  and  $(-0.067, \pm 0.025, 0.042)(1/\text{\AA})$  and energy  $E=-0.003$  eV, as shown in Fig 3b. To characterize the topological nature of these nodes, we have calculated their chirality. We find that two of the nodes have chirality +1 (red) and the other two have chirality -1 (blue), which we tentatively interpret as 4 Weyl nodes originating from the two original Dirac nodes. Note that the nodes are closer to the  $\Gamma$  point compared to the location of the Dirac nodes in the pure  $Cd_3As_2$ .

To further confirm that these nodes are indeed Weyl points, we have calculated the Berry curvature, since a Weyl point acts as a source or a drain of Berry curvature in momentum space. In Fig. 4(a,b) we have plotted the curvature in the  $k_x - k_z$  plane, at fixed  $k_y = 0.025(1/\text{\AA})$ , around the two Weyl nodes WP1 and WP3 ( Fig 3b), respectively. It is evident that WP1 and WP3 act as a source and drain, respectively, as the Berry curvature diverges at the WPs, which supports the conclusion that these are two Weyl nodes of opposite chirality. In Fig. 4(c), we have plotted the surface states spectra

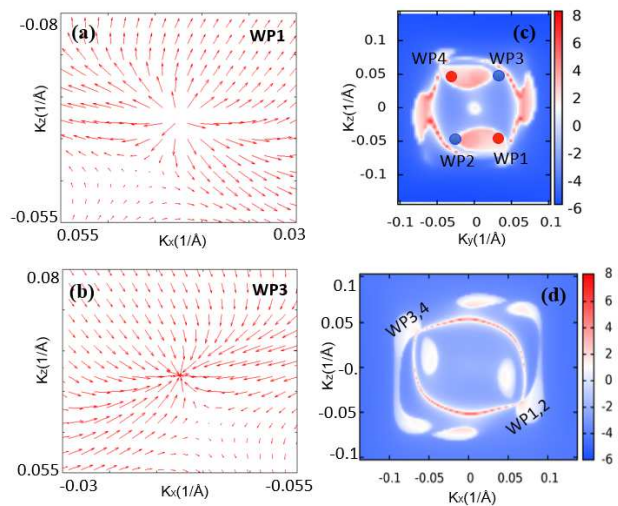


FIG. 4. The Berry curvature in the  $k_x - k_z$  plane, at fixed  $k_y = 0.025(1/\text{\AA})$  for the doping case considered in Fig. 3. (a) and (b) The Berry curvature in the neighborhood of WP1 and WP3 of Fig. 3 with opposite chiralities, respectively. the curvature diverges at the location of the WPs. (c) Fermi arc surface states projected onto the (100) surface. (d) The Fermi arc states projected onto (010) surface.

on the (100) surface at constant  $E=-0.003$  eV. We can clearly see two Fermi arcs, emanating from two different Weyl points, although some bulk states are also present. We have also plotted surface states on (010) surface in Fig. 4(d). The WPs (WP1, WP2) and (WP3, WP4) are projected onto the the same points on this surface, therefore, the two arc states appear to emanate from the same

point.

The bands are fully gapped on the  $k_z = 0$  TRIP, and  $Z_2 = 1$  on this plane, which indicates a non-trivial gap. This opens up the possibility of observing a quantum spin Hall effect on this plane, similar to that one predicted for the TaAs WSM family[57]. Our calculations clearly demonstrate that the insertion of a single Zn impurity in the  $Cd_3As_2$  unit cell causes a topological phase transition to a Weyl phase, which is more robust than the DSM phase.

### 3. Broken IS symmetry: coexisting of Dirac and Weyl phases

We finally discuss the last example of nonmagnetic doping in  $Cd_3As_2$ , consisting of a  $\delta$ -type doping of Zn impurities (see Fig. 1) such that IS is broken while the  $S_{4z}$  screw symmetry is preserved. The dopants substitute twelve Cd atoms in two different parallel planes perpendicular to the tetragonal axis (along the  $z$  direction), resulting in  $I4_2mc$  space group (associated point group,  $C_{4v}$ ). This space group contains the  $M_{xz}$  and  $M_{yz}$  mirror planes along with the  $S_{4z}$  screw axis.

This is a particularly interesting case. Since  $M_{yz}$  and  $S_{4z}$  are symmetries of this space group, they commute with the Hamiltonian:  $[M_{yz}, H] = 0$ ,  $[S_{4z}, H] = 0$ . However, these two symmetries do not commute with each other, but rather they *anticommute*,  $\{M_{yz}, S_{4z}\} = 0$ . The anti-commutation of two symmetry operators of a Hamiltonian plays a crucial role in generating degeneracies of the energy bands. To elaborate, let  $\psi_s$  is an eigenstate of  $S$  with eigenvalue  $s$ , which is also an eigenstate of  $H$  with energy  $E$  i.e.  $S\psi_s = s\psi_s$  and  $H\psi_s = E\psi_s$ . Then,  $H(M\psi_s) = M(H\psi_s) = E(M\psi_s)$ . Therefore,  $M\psi_s$  is also an eigenstate of  $H$  with energy  $E$ . Now, since  $S$  and  $M$  anticommute,  $S(M\psi_s) = -M(S\psi_s) = -s(M\psi_s)$ . Therefore,  $\psi_s$  and  $M\psi_s$  are two orthogonal eigenstates of  $H$  with the same energy  $E$ , that is,  $E$  is degenerate. The presence of these two anti-commuting symmetry operators ensures that all bands are two-fold degenerate along the tetragonal axis,  $k_z$  (Z- $\Gamma$ -Z path where band inversion occurs in the pure  $Cd_3As_2$ ). Because of the maintained  $S_{4z}$  screw symmetry, the Dirac points of the DSM phase are still present on this axis in this doped system.

Furthermore, the breaking of IS gives rise to the possibility of two-fold degenerate nodes, possibly Weyl points, away from the tetragonal axis. These nodes cannot be directly generated from the original Dirac points, as in the case of a single Zn doping, because in this case the original Dirac nodes are still present in the system. Therefore, this particular implementation of the impurities, opens up the possibility of observing a Dirac+Weyl coexisting phase, similar to the one recently discovered in polar hexagonal  $ABC$  Crystal SrHgPb[40].

For a detailed analysis, we have performed calculations for both relaxed and unrelaxed structures. Fig 5 shows the bandstructure for the unrelaxed structure. Here by

*unrelaxed* we mean the system where the impurities have been inserted in the *relaxed* pure  $Cd_3As_2$  crystal, without carrying out any further relaxation. We can clearly see the presence of a four-fold Dirac node with zero chirality (derived from WannierTools) along Z- $\Gamma$ -Z path for which the double degeneracy is preserved. This is similar to the pure  $Cd_3As_2$  case, however, it differs in an important way. In pure  $Cd_3As_2$ , the linearly dispersed states emanating from the Dirac node form a doubly-degenerate 3D Dirac cone. But in this case, it can only form a doubly-degenerate cone on a 2D plane (the shaded plane shown in the inset of Fig. 5) for the states along the  $k_z$ -axis. Away from Z- $\Gamma$ -Z path the bands are no longer doubly degenerate and split into two nondegenerate cones (the gray cone, and the yellow cone inside it as shown in the inset). To search for the nodes, we need to look for

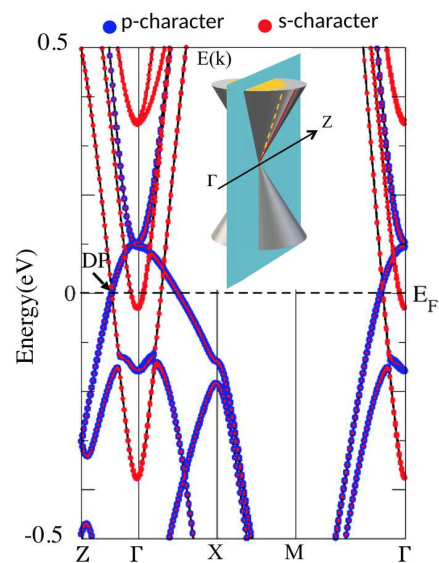


FIG. 5. The bandstructure of Zn-doped  $Cd_3As_2$  with broken IS but with preserved  $S_{4z}$  screw symmetry. The projections of As  $p$  and Cd  $s$  states are shown in blue and red, respectively. The black arrow indicates the DP on the Z- $\Gamma$  path along which the double degeneracy of the bands is preserved. The inset shows a schematic of the bands around the DP, plotted in a  $k$ -plane containing the Z- $\Gamma$  axis. The doubly degenerate states of the cone are those that lie on the shaded 2D plane.

band-touching points at generic points in the full BZ, not necessarily on the high-symmetry axis, which is difficult to achieve using DFT. To facilitate this search, we have constructed a TB model in the Wannier function basis using the Wannier90 code, and then we have used WannierTools to search for nodes. We found two band touchings along the tetragonal axis at  $\mathbf{k} = (0, 0, \pm 0.11)(1/\text{\AA})$ , namely the expected Dirac points, and eight new two-fold degenerate nodes in the  $k_z = 0$  plane, as shown in Fig 6a. The Dirac nodes are essentially at the Fermi energy, but the Weyl nodes lie about 16 meV above the Fermi level. To investigate whether these eight nodes are Weyl nodes, we have calculated the chirality of each

node, which shows that four of the nodes have chirality +1 (red dots) and the remaining four have chirality -1 (blue dots), suggesting that they are indeed Weyl nodes. The Dirac nodes, on the other hand, have chirality zero. For further evidence, we have plotted the Berry curvature on the  $k_z = 0$  plane, zoomed around two nodes of opposite chirality, as shown in Fig 6b. It clearly shows source-like and drain-like divergences of the curvature around each node, which is a characteristic feature of the Weyl nodes. In Fig 6c we have plotted the surface states projected onto (001) plane at  $E=0.016$  eV. While small bulk states are still present at this energy, it is also evident there are surface states connecting different pairs of Weyl nodes. These results indicate that

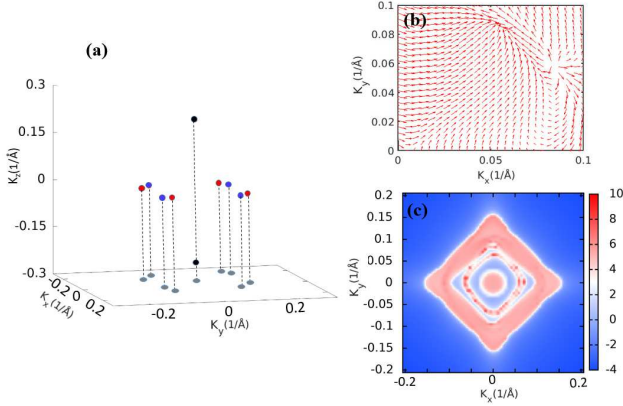


FIG. 6. (a) Dirac+Weyl coexisting phase: a pair of Dirac nodes on the  $k_z$ -axis and four pairs of Weyl nodes on the  $k_z = 0$  plane (blue and red dots represent Weyl nodes of opposite chirality). (b) The Berry curvature around a pair of Weyl nodes of opposite chirality, showing the divergence of the curvature at the nodes. (c) The Fermi surface states projected onto the (001) surface at  $E=0.016$  eV above the Fermi level.

this unrelaxed  $(Cd_{1-x}Zn_x)_3As_2$  ( $x=0.5$ ) system is a very unusual and interesting topological system in which both Dirac and Weyl nodes coexist, resulting in a new topological phase that is a mixture of DSM-like and WSM phases (We say, DSM-like because, as we discussed above, the bands crossing at these nodes are doubly-degenerate only along the  $Z - \Gamma - Z$  path).

In order to further elucidate this mixed phase, we formulate a low-energy effective Hamiltonian  $H(\mathbf{k})$  using a four-band  $\mathbf{k} \cdot \mathbf{p}$  model. We consider the conduction and valence bands around the  $\Gamma$  point where Cd-5s and As-4p states are inverted. In presence of spin-orbit coupling, these states at the  $\Gamma$  point can be specified by the eigenvalues of the total angular momentum operators  $\mathbf{J}^2$  and  $J_z$ :  $|S_{1/2}, \pm 1/2\rangle$ , heavy hole states  $|P_{3/2}, \pm 3/2\rangle$ , light hole states  $|P_{3/2}, \pm 1/2\rangle$  and split-off states  $|P_{1/2}, \pm 1/2\rangle$ . The light hole and split-off states lie further below the Fermi level; therefore, in order to construct the minimal four-band model we have considered only the  $|S_{3/2}, +3/2\rangle$ ,  $|S_{1/2}, +1/2\rangle$ ,  $|S_{1/2}, -1/2\rangle$ ,

and  $|P_{3/2}, -3/2\rangle$  states.

Applying  $\mathbf{k} \cdot \mathbf{p}$  perturbation theory to these states up to the second order, and making use of the crystal symmetries, the Hamiltonian  $H(\mathbf{k})$  takes the following form [58]

$$H(\mathbf{k}) = \epsilon_0(\mathbf{k}) + \begin{pmatrix} -M(\mathbf{k}) & Ak_- & 0 & 0 \\ Ak_+ & M(\mathbf{k}) & Dk_- & 0 \\ 0 & Dk_+ & M(\mathbf{k}) & -Ak_- \\ 0 & 0 & -Ak_+ & -M(\mathbf{k}) \end{pmatrix} \quad (1)$$

where  $\epsilon_0(\mathbf{k}) = C_0 + C_1k_z^2 + C_2(k_x^2 + k_y^2)$ ,  $M(\mathbf{k}) = M_0 - M_1k_z^2 - M_2(k_x^2 + k_y^2)$  and  $k_{\pm} = k_x \pm ik_y$ . The parameter  $D$  reflects the breaking of IS. If  $D = 0$ , Eq. 1 can be linearized about the DP to obtain the Dirac Hamiltonian of pure  $Cd_3As_2$ . The energy dispersions are

$$E_1^{(\pm)}(\mathbf{k}) = \epsilon_0(\mathbf{k}) + \frac{1}{2} \left[ \pm D \sqrt{k_x^2 + k_y^2} \pm \sqrt{(4A^2 + D^2)(k_x^2 + k_y^2) \pm 4M(\mathbf{k})D \sqrt{k_x^2 + k_y^2} + 4M(\mathbf{k})^2} \right]$$

$$E_2^{(\pm)}(\mathbf{k}) = \epsilon_0(\mathbf{k}) + \frac{1}{2} \left[ \pm D \sqrt{k_x^2 + k_y^2} \mp \sqrt{(4A^2 + D^2)(k_x^2 + k_y^2) \pm 4M(\mathbf{k})D \sqrt{k_x^2 + k_y^2} + 4M(\mathbf{k})^2} \right] \quad (2)$$

The coefficients in Eq. 1 are obtained by fitting to the DFT bands and are listed in Table I. Fig. 7a compares the bands from DFT and  $\mathbf{k} \cdot \mathbf{p}$  model, which are in a good agreement. Along the  $Z-\Gamma-Z$  axis  $(0, 0, k_z)$  these dispersion energies are two-fold degenerate, and when they cross, they form a Dirac node. The positions of the Dirac nodes obtained from Eq. 2 are  $(0, 0, \pm \sqrt{\frac{M_0}{M_1}})$ . To check the topological nature of these nodes, in particular if they have a chiral charge, we perform a Taylor expansion of the dispersion around the Dirac point. Keeping only terms linear in the variation  $\delta\mathbf{k}$ , we obtain

$$E_1^{(\pm)}(\delta\mathbf{k}) = \pm |v_{1xy}(\delta k_x \hat{x} + \delta k_y \hat{y}) + v_z \delta k_z \hat{z}| \quad (3)$$

$$E_2^{(\pm)}(\delta\mathbf{k}) = \mp |v_{2xy}(\delta k_x \hat{x} + \delta k_y \hat{y}) + v_z \delta k_z \hat{z}|$$

where the two in-plane velocities are  $v_{1xy} = \frac{1}{2}(+D + \sqrt{4A^2 + D^2})$ ,  $v_{2xy} = \frac{1}{2}(-D + \sqrt{4A^2 + D^2})$ , with  $v_{1xy} > v_{2xy} > 0$ , and  $v_z = 2\sqrt{M_0M_1}$ . The two energy pairs  $E_1^{(\pm)}$  and  $E_2^{(\pm)}$  in Eq. 3 are the solutions of the two  $2 \times 2$  Weyl Hamiltonians  $H_{WP,1}(\delta\mathbf{k}) = \mathbf{V}_1(\delta\mathbf{k}) \cdot \boldsymbol{\sigma}$ , and  $H_{WP,2}(\delta\mathbf{k}) = -\mathbf{V}_2(\delta\mathbf{k}) \cdot \boldsymbol{\sigma}$  respectively, where  $\mathbf{V}_i(\delta\mathbf{k}) = v_{ixy}(\delta k_x \sigma_x + \delta k_y \sigma_y) + v_z \delta k_z \sigma_z$ ,  $i = 1, 2$  and  $\boldsymbol{\sigma}$ 's are Pauli matrices. The minus sign in front of  $H_{WP,2}$  is important: it implies that for each  $\mathbf{k}$  the two eigenstates corresponding to a given sign of the dispersion are swapped with respect to  $H_{WP,1}$ . Then the full  $4 \times 4$  Hamiltonian around the Dirac point can be written in the form:

$$H_{DP}(\delta\mathbf{k}) = \begin{pmatrix} \mathbf{V}_1(\delta\mathbf{k}) \cdot \boldsymbol{\sigma} & 0 \\ 0 & -\mathbf{V}_2(\delta\mathbf{k}) \cdot \boldsymbol{\sigma} \end{pmatrix}, \quad (4)$$

which corresponds to two coincident Weyl nodes of opposite chirality. Therefore, the Dirac nodes of this coexisting phase have chiral charge zero. It is also evident from the Hamiltonian  $H_{DP}(\delta\mathbf{k})$  that the double degeneracy of the Dirac cone is preserved only along  $k_z$  but splits for  $\mathbf{k}$ -points away from this tetragonal axis, as obtained from the DFT calculations (Fig. 5).

In addition to the Dirac nodes, the model, with the *same* parameters, also predicts the existence of four pairs of nodes on the  $k_x - k_y$  plane. As shown in Fig 7b, the position of these nodes essentially coincides with the positions the four pairs of Weyl nodes obtained from the DFT calculations. The small difference is due to the fact that we are using a simplified model with just four bands, which cannot capture all the details of the DFT results.

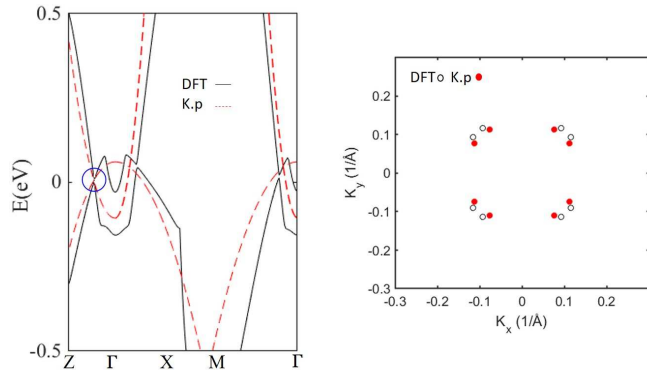


FIG. 7. (a) Comparison of the DFT band structure and the bandstructure given by the  $\mathbf{k} \cdot \mathbf{p}$  model for the coexisting phase. The blue circle indicates the Dirac point. (b) Position of the Weyl nodes obtained from DFT (open circles) and the  $\mathbf{k} \cdot \mathbf{p}$  model (filled red circles).

TABLE I. Coefficients for the four-band  $\mathbf{k} \cdot \mathbf{p}$  model of Eq. 1 obtained by fitting the DFT results.

$C_0$	$C_1$	$C_2$	$A$	$M_0$	$M_1$	$M_2$	$D$
(eV)	(eV-Å <sup>2</sup> )	(eV-Å <sup>2</sup> )	(eV-Å)	(eV)	(eV-Å <sup>2</sup> )	(eV-Å <sup>2</sup> )	(eV-Å)
-0.0250	28.0234	145.0648	-0.0060	-0.0833	-82.9471	-179.7532	0.2000

The effective model can be also used to investigate the stability of the coexisting phase. We find that this phase is most sensitive to the parameters  $A$  and  $D$ , which are proportional to the in-plane components of the velocity. Our calculations show that for a small range of  $A$  (-0.002 - 0.007) eV-Å and  $D$  (0.06 - 0.265) eV-Å both Dirac and Weyl nodes remain stable, if all other parameters are kept fixed to their optimal values listed in Table I. We can imagine that changing these parameters might correspond to acting externally on the system, e.g., by applying an external strain, while maintaining the symmetry of the system. Although establishing a direct connection between the parameters of the  $\mathbf{k} \cdot \mathbf{p}$  model and external strain is not straightforward, these results indicate that at least for a small range of the parameters that might be

controlled externally, the coexisting phase of DSM and WSM should remain stable.

#### 4. Effect of external strain on the coexisting phase

To further investigate the stability of this mixed phase, we have relaxed the structure for both the cell parameters and the atomic positions. Relaxation reduces the cell parameter to  $a = b = 16.567031$  and  $c = 23.487859$  bohr and brings the As layer closer to the Zn layer (further away from the Cd layer) but the bandstructure is similar to that of unrelaxed case. To search for the nodes in the full BZ, we have followed the same procedure used above. In this case we have found only the Dirac nodes along the tetragonal axis (slightly moved along the line), whereas the Weyl nodes on the  $k_z = 0$  plane have disappeared. Since the bands are now gapped on  $k_z = 0$  plane, we have calculated the  $Z_2$  invariant, which shows the plane is topologically trivial. Furthermore, since  $k_z = 0$  plane is not a mirror plane of the  $C_{4v}$  point group, this plane cannot be characterized by mirror Chern number either. Therefore, in this particular case, the non-trivial topology related to the Dirac phase is broken. Although the four-fold degenerate nodes are still present in the system protected by the  $S_{4z}$  screw symmetry, no other topological aspects are found in the system, resulting in a trivial semimetal.

The relevant question now is whether or not the Dirac+Weyl mixed phase can exist in more general conditions (as our  $\mathbf{k} \cdot \mathbf{p}$  model suggests), in particular for physical configurations where the atomic positions are relaxed, which can be realized experimentally. In order to realize such a coexisting phase, we need to consider an additional degrees of freedom, which can induce additional accidental double degeneracies away from the Z-Γ-Z axis.

Since the unit-cell lattice constants  $a$ ,  $b$ , and  $c$  of the relaxed system are smaller than the ones of the unrelaxed structure, we have investigated whether or not the coexisting Dirac+Weyl phase reappears when the unit cell size is progressively increased from the relaxed one. This procedure is supposed to describe an applied external strain. Specifically, in these calculations we have simulated an external strain by acting on the cell in the following way: we first modify (increase) the cell parameters, and then we relax the atomic positions for the new cell parameters. We have focused our search by varying the applied strain in a limited area of the parameter space, namely by increasing the lattice constants  $a = b$  while keeping the ratio  $c/a$  equal to the value of the relaxed system  $c/a = 1.417747$ . The different strained systems that we considered are listed in Table II. Note that the first entry in this table is for the case in which  $a$  and  $b$  take the value of the unrelaxed system but the atomic positions have been relaxed.

We should remark that this particular approach of applying strain may be difficult to realize experimentally



but here we would like to investigate, theoretically, whether by progressively increasing the strain close to the unrelaxed system parameters, the trivial phase of the relaxed structure eventually changes into a topological Dirac phase. We are interested in how the band structure changes under strain, looking, in particular, at the gaps around the Fermi energy which, at some point, must close in order for the topology to change. A more realistic modeling of strain would certainly be required to make predictions that can be verified experimentally. However, our simplified approach can still provide insight into the possibility of obtaining and controlling the co-existing phase by external probes.

TABLE II. Applied strain in  $Cd_3As_2$ . Strain is modeled by changing the lattice constants  $a$ ,  $b$  and  $c$  under the conditions that  $a = b$ , and the ratio  $c/a$  is kept fixed and equal to the value of the relaxed doped structure, 1.42. For the case of the first row (strain I),  $a = b = 17.27$  equal to the value of the unrelaxed system, but the atomic positions have been relaxed.

Structure	Lattice constant a = b (bohr)	Stress (Kbar)		phase
		along x, y	along z	
I	17.27	-44.90	-43.43	Trivial
II	17.30	-45.00	-42.56	DSM
III	17.34	-47.09	-44.47	DSM
IV	17.45	-51.19	-47.97	DSM
V	17.62	-55.36	-50.23	DSM

Although the qualitative behavior of the bands is very similar for different values of the strain, topological phase transitions can occur due to some changes around the Fermi level. In particular, as we show below, the strained systems I and V in table II have different topological characters; since the four-fold band touchings along the tetragonal axis, i.e., the original Dirac points, are always present in all strained systems, the changing of the topology must occur through an intermediate phase, in which energy gaps must close somewhere else in the BZ.

In Fig. 8 the band structure of “strained system I” is plotted along the  $Z-\Gamma-X-M-\Gamma$  path. This strain corresponds to the case where the lattice constants  $a$  and  $b$  are equal to the value of the *relaxed pure*  $Cd_3As_2$  (which we therefore refer to as *unrelaxed* for the doped system). Away from the Fermi level, the bands are similar to the fully relaxed system. Close to the Fermi energy we can see that, besides the usual four-fold band touching along  $Z-\Gamma$ , some  $k$ -points in the  $k_z = 0$  plane along the  $\Gamma-X$  and  $\Gamma-M$  path present what seems to be band touchings. A more detailed analysis reveals that these are actually gapped points, with a small gap of  $\Delta E \sim 0.5$  meV along  $M-\Gamma$ , even smaller than the one present in the total relaxed system. Furthermore, the node search with WannierTools did not find any new nodes in the BZ. The  $Z_2$  calculations on the  $k_z = 0$  TRIP, whose WCC evolution is shown in Fig. 8b, reveals that the system has the same trivial topology of the fully relaxed system. This is because a generic horizontal line cuts the WCC branches in an even number (two) or zero times.

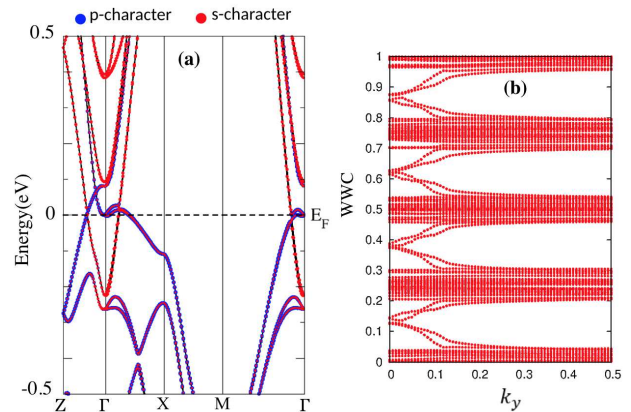


FIG. 8. (a) Band structure of the strained system I (see Tab. II) showing the Dirac node on the  $Z-\Gamma$  high-symmetry line. (b) Evolution of the WCCs in the  $k_z = 0$  TRIP, demonstrating the trivial topology of this plane.

In order to see how these gaps along the  $\Gamma-X$  change with different strains, we plot the evolution of the bands along the  $\Gamma-X$  zoomed around the gaps, for all the five strained systems of Tab. II. As it is shown in Figs. 9, the gap is getting smaller until the third case, after which it starts to increase signaling that if there is any band closings, this must happen at an intermediate value of the strain. The same thing can be shown for the  $\Gamma-M$  direction. Among the strained systems II-IV in Table II, the strained system II gives the smallest gap of 0.4 meV between the conduction and the valence band along the  $\Gamma-X$  and  $\Gamma-M$  lines.

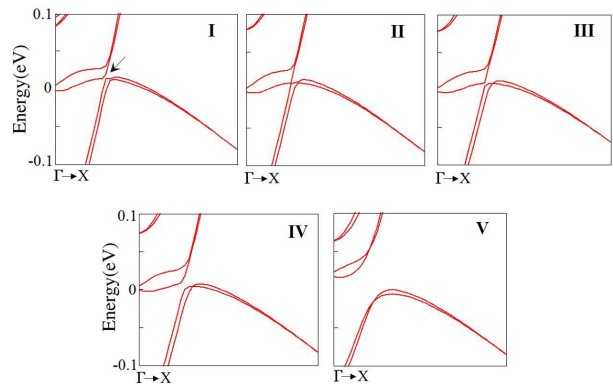


FIG. 9. Energy bands along  $\Gamma-X$  in a region close to  $\Gamma$ , which shows how the gap between the conduction and the valence bands changes with the strain. The different panels I-V refer to the five strain realizations of Table II. The arrow in the panel I marks the point of closest approach of the conduction and valence bands.

The topological analysis shows that the strained systems II-IV are already in the non-trivial DSM phase of the pure  $Cd_3As_2$  system (see Table II). Since the topology changes from the trivial semimetal phase of strain I to the non-trivial DSM phase of strain II, we deduce

that a band gap closing must necessarily take place for an intermediate value of the strain. Because of the maintained  $S_{4z}$  for this doped system, such a node in the band structure will have three other copies at rotated positions, and we expect these 4 nodes to be of Weyl type. Being unable to pin-point the exact value of the strain corresponding to the band closing, we are unable to conclusively confirm via a topological analysis that the transition between the two phases indeed takes place via the mixed Weyl+Dirac phase that we have discovered for the unrelaxed system. However all these features indicate that this coexisting phase is the most likely occurrence, which is also supported by the model Hamiltonian discussed in Sec. III A 3.

A phase diagram summarizing the topological evolution of  $(Cd_{1-x}Zn_x)_3As_2$  ( $x = 0.5$ ) as a function of applied strain is shown in Fig. 10. Here the value of the applied strain is expressed in terms of the ratio  $r = a_{\text{strained}}/a_{\text{relaxed}}$ , which tells us how much the first lattice parameter of the strained cell ( $a_{\text{strained}}$ ) is enlarged relatively to the one of the totally relaxed system ( $a_{\text{relaxed}}$ ).

Summarizing the results for the  $(Cd_{1-x}Zn_x)_3As_2$  ( $x=0.5$ ) system, we found that this doped system that breaks IS but maintains both the  $S_{4z}$  symmetry and TRS can exist in three distinct topological phases: (i) a topologically trivial semimetal phase, still possessing two four-fold nodal points on the  $\Gamma - Z$  axis; (ii) a topological nontrivial DSM phase, characteristic of the pure system; (iii) a novel mixed Weyl+Dirac phase, first found in the unrelaxed  $(Cd_{1-x}Zn_x)_3As_2$  system, where lattice constants and atomic positions of pure  $Cd_3As_2$  were used. This mixed Weyl+Dirac phase also appears at the topological phase transition point between the trivial and DSM phase, induced by an applied external strain, as shown in Fig. 10.

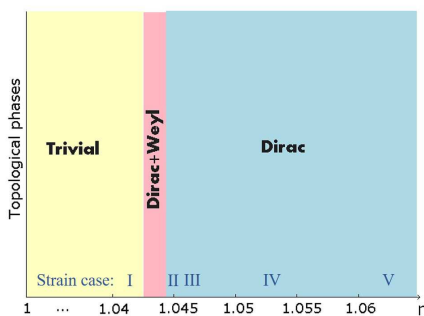


FIG. 10. Phase diagram of the topological evolution of the system, in terms of the ratio  $r = a_{\text{strained}}/a_{\text{relaxed}}$ . The parameters  $a_{\text{strained}}$  and  $a_{\text{relaxed}}$  are the  $a$ -lattice constants of the totally relaxed ( $a_{\text{relaxed}} = 16.567031$  bohr) and of a strained system, respectively.

At this point we are not able to conclusively assess from the DFT calculations whether or not the mixed phase can exist for a finite albeit small range of the parameters that we use to model the strain in the system. For

the systems considered in Table II, the value of  $c/a$  is kept fixed and equal to the value of the relaxed doped  $(Cd_{1-x}Zn_x)_3As_2$ . Changing this parameter can allow further flexibility to induce nodal points leading to a mixed Weyl+Dirac phase. Indeed, the model shows that despite changing some of the parameters in the system, the mixed phase can still be maintained.

## B. Magnetic impurity in $Cd_3As_2$

Magnetic doping of topological DSMs is of great interest for both fundamental and application reasons, since the magnetic Weyl phase that can arise due to the broken TRS may support topological phenomena such as the quantum anomalous Hall effect. In this section we discuss the effects of magnetic doping in  $Cd_3As_2$ . We have investigated two cases: i) TRS is broken but IS is preserved ii) both TRS and IS are broken. In both cases, we obtain Weyl phases, which are discussed below. The DFT calculations are performed using both GGA and GGA+U with  $U_{\text{eff}}=4$  eV, but here we mostly discuss the results when  $U$  is included.

The stability of  $Cd_3As_2$  doped with different transition metal magnetic impurities has been investigated and confirmed recently[59] by calculating the formation energy. In our study we have used Mn-doped  $Cd_3As_2$  since Mn has largest magnetic moment. To preserve IS, we have introduced two Manganese (Mn) atoms at two Cd sites that are related by inversion in a 40-atom cell, corresponding to  $\sim 8\%$  impurity concentration. The symmetry of the system reduces to  $P2_1/m(C_{2h}^2)$ , which contains a mirror plane,  $\sigma_h$  and a  $C_2$  rotational symmetry along with inversion. This structure is the same as the one with two Zn impurity discussed in Sec III A 1, except that TRS is broken in the present case due to the magnetic impurity.

Fig. 11a shows the bandstructure of Mn-doped  $Cd_3As_2$ . The correlation among Mn  $d$  electrons pushes the occupied  $d$  states 5 eV below the Fermi level, as evident from the density of states (DOS) shown in Fig. 11b. Since the correlation strongly localizes the  $d$  electrons of Mn, the hybridization with As  $p$  states becomes negligible. Therefore, the electronic properties around the Fermi level are essentially determined by As  $p$  and Cd  $s$  states. It is also evident from the bandstructure that close to the Fermi level As  $p$  states are higher in energy compared to Cd  $s$  states around the  $\Gamma$  point, as in the case of pure  $Cd_3As_2$  (Fig 2a), indicating that band inversion is still preserved in the presence of Mn impurities. The magnetic moment of Mn atoms are  $4.5 \mu_B$ , which is  $0.5 \mu_B$  larger than the corresponding GGA value. Although the  $d$  states are absent at the Fermi level, the magnetization associated with these states play a crucial role in the topological properties by lifting the spin degeneracies of the bands.

Since the TRS is broken, the double degeneracies of the bands are lifted. Furthermore, the lack of screw symmetry also breaks the degeneracy along the tetrago-

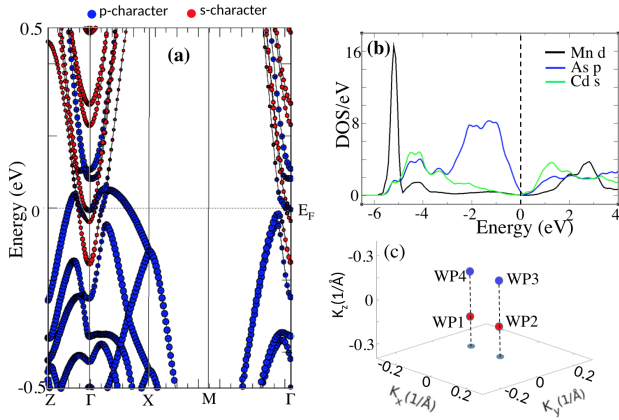


FIG. 11. (a) Bandstructure of Mn-doped  $Cd_3As_2$ . The bands around the Fermi energy are predominantly of As  $p$  (blue) and Cd  $s$  (red) characters. (b) Projected DOS showing the contribution of different atoms in the system. (c) Position of the four Weyl nodes (WP1-WP4), emerging as a result of broken TRS. The red (blue) dots represent nodes with +1 (-1) chirality.

nal axis. Consequently, the original four-fold degenerate Dirac points along  $Z - \Gamma$  line disappear. But the presence of Mn impurity introduces a splitting of the bands which may give rise to new crossing points and consequently new nodes at generic  $\mathbf{k}$  points. Therefore, we have searched for the nodes in the full BZ, and have found four nodes just 8 meV below the Fermi level. The position of the nodes are close to the Dirac point of pure  $Cd_3As_2$  on the  $k_y=0$  plane with two at  $(\pm 0.057, 0.0, -0.076)(1/\text{\AA})$  (WP1, WP2) and the other two at  $(\pm 0.057, 0.0, -0.076)(1/\text{\AA})$  (WP3, WP4), as shown in Fig. 11c. The calculation of the chirality shows that WP1 and WP2 have +1 chirality (red) whereas WP3 and WP4 have -1 chirality (blue). Therefore, these nodes are Weyl nodes. The result is consistent with the expectation that breaking of IS or TRS leads to the transition to a WSM phase.

It is interesting to note that unlike the Weyl phase obtained by non-magnetic impurity (Sec III A 2), in this case the two Weyl points below (above) have the same chirality, which can be understood from the symmetry properties of the Berry curvature,  $\mathbf{\Omega}(\mathbf{k})$ . As mentioned above, this doped system contains both inversion and  $\sigma_h$  mirror plane. Under IS,  $\mathbf{\Omega}(\mathbf{k})$  is even i.e.  $I : \mathbf{\Omega}(-\mathbf{k}) = \mathbf{\Omega}(\mathbf{k})$ , and for  $\sigma_h$  plane only the  $x$  and  $y$  components of  $\mathbf{\Omega}(\mathbf{k})$  change sign i.e.  $\sigma_h : (\Omega_x, \Omega_y, \Omega_z)(k_x, k_y, -k_z) = (-\Omega_x, -\Omega_y, \Omega_z)(k_x, k_y, k_z)$ . Consequently, since WP1 and WP3 are inversion symmetric partners, they have opposite chiralities. Also, since WP1 (WP2) and WP4 (WP3) are related by  $\sigma_h$ , they must also have opposite chirality.

Because of broken TRS, the topological properties of the crystal planes cannot be characterized by the  $Z_2$  invariant. Instead, we have calculated the Chern number for the planes using WCC methods, which is similar to

the calculation of  $Z_2$  invariant, except that in this case we use a full path in momentum plane. Since the nodes lie on the  $k_y=0$  plane, we have calculated the Chern number for  $k_x = 0$  and  $k_z = 0$  planes. Our calculation show that the Chern number is 1 only for the  $k_x = 0$  plane, which signifies that this plane may be viewed as a 2D Chern insulator. Therefore, we expect this particular system to support the Quantum Anomalous Hall Effect, as discussed in section I.

Finally, we break both TRS and IS by substituting only one Cd by one Mn impurity. Symmetry is further reduced to  $C_s$  point group, which contains only a  $\sigma_h$  mirror plane. The bandstructure is very similar to the one for 2 Mn impurity shown in Fig. 11a except that a few additional levels appear due to the reduced symmetry. As before we have searched for nodes in the BZ, and as expected we have found no Dirac nodes. Instead, we have found four Weyl nodes, two at  $\mathbf{k}$ -points  $(0, \pm 0.047, \mp 0.083)(1/\text{\AA})$  at 35 meV above the Fermi level with opposite chirality, and two nodes at  $\mathbf{k}$ -points  $(0, \pm 0.056, \mp 0.039)(1/\text{\AA})$  at 15 meV below the Fermi level, also with opposite chirality. While this system may be viewed as a WSM, it may not be a very promising system for practical purposes, since the nodes are rather far away from the Fermi level.

We also would like to remark that, in principle, one might think of inducing a coexisting phase by breaking TRS while preserving IS,  $S_{4z}$  the and mirror symmetries. However, such a realization requires a high concentration of Mn doping, which is likely to turn the system into a magnetic metal with trivial topological properties.

A concise summary of all the results for doped  $Cd_3As_2$  obtained in this work is presented in Table III.

TABLE III. Summary of the results for different topological phases induced by different impurity-doping realizations in  $Cd_3As_2$ .

Impurity	Symmetry	Topological properties
0	TRS + IS + $C_4$	DSM phase Two DPs on the $k_z$ axis. $Z_2=1$ only at $k_z = 0$ TRIP.
2 Zn (9%)	TRS + IS	Topological insulator phase A gap of 15 meV at the original DPs. $Z_2=1$ for $k_x, k_y, k_z = 0$ TRIPs.
1 Zn (4%)	TRS	WSM phase 2 DPs splits into 4 Weyl nodes $Z_2=1$ only at $k_z = 0$ TRIP
12 Zn (Unrelaxed) (50%)	TRS + $C_4$	Coexisting DSM and WSM phase. Two Dirac nodes on $k_z$ and eight Weyl nodes $k_z = 0$ plane.
12 Zn (Relaxed)	TRS + $C_4$	Trivial semi-metal phase Two Dirac nodes on $k_z$
2 Mn (8%)	IS	Magnetic WSM phase 4 Weyl nodes, two with chirality +1 (-1) below (above) $k_z = 0$ plane
1 Mn (4%)	All broken	Magnetic WSM phase 4 Weyl nodes on $k_x = 0$ plane but not related by IS or TRS.

#### IV. TOPOLOGICAL PHASE TRANSITIONS IN $Na_3Bi$ DSM

In this section we turn our attention to the topological properties of Sb doped  $Na_3Bi$  DSM. Pure  $Na_3Bi$  belongs to the hexagonal  $P6_3/mmc$  ( $D_{6h}^4$ ) space group, which is characterized by IS,  $6_3$  screw symmetry  $S_{6z}$  along with  $C_3$  symmetry. As we will see below, the  $C_3$  symmetry has important consequences in preserving the degeneracy of the bands when the  $S_{6z}$  symmetry is lifted by doping. To investigate how doping modifies the topological properties, we first calculated the electronic structure and topology of pure  $Na_3Bi$ . After relaxation, the lattice constants increase from the experimental value of  $a=b=10.29$  and  $c=18.25$  bohr to  $a=b=10.34$  and  $c=18.38$  bohr. The bandstructure of this relaxed system, plotted in Fig 12a, shows that the two-fold degenerate valence band crosses with conduction band on the  $k_z$  axis (A- $\Gamma$  path) and forms a Dirac node, in agreement with previous work[11]. As in the case of  $Cd_3As_2$ , there are two Dirac nodes symmetrically placed around the  $\Gamma$  point on the hexagonal axis at  $(0, 0, \pm 0.086)$  ( $1/\text{\AA}$ ) with zero chirality.

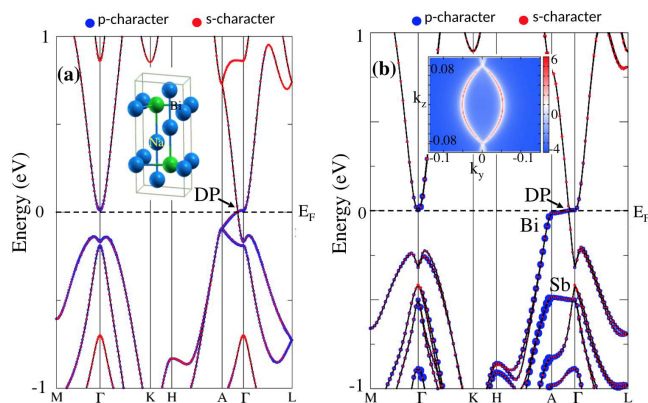


FIG. 12. (a) The bandstructure of  $Na_3Bi$  DSM indicating the position of the Dirac point on the  $k_z$  axis along the A- $\Gamma$  path. The projections of the Bi, Sb  $p$  and Na  $s$  states are shown in blue and red, respectively. The inset shows the unit cell of  $Na_3Bi$ . (b) The bandstructure of  $Na_3Bi$  doped with a single Sb impurity in the unit cell, breaking both IS and  $S_{6z}$ . The Fermi arc surface states on the  $[010]$  surface are shown in the inset.

To study the effect of non-magnetic impurities on the topological properties, we have substituted one Bi atom with one Sb, which is isoelectric to Bi. Since there are only two Bi atoms in the unit cell, this doping corresponds to 50% impurity concentration. The space group of the system, consequently, changes to  $P\bar{6}m2$  (or  $D_{3h}^1$ ), which lacks IS but contains a Mirror plane  $M_{110}$  perpendicular to  $(110)$  direction as well as the  $C_3$  rotational symmetry. Unlike pure  $Na_3Bi$ , the relaxation of the doped structure reduces the cell parameters to  $a = b = 10.23$  and  $c = 18.21$  bohr compared to the experimental cell parameters of pure  $Na_3Bi$  mentioned above. The

bandstructure in Fig. 12(b) shows that the  $p$  states of Sb lies about 0.5 eV below the Bi  $p$  states. Therefore, the electronic properties around the Fermi level are essentially determined by Bi  $p$  and Na  $s$  states. It is also evident that the band inversion is still preserved along A- $\Gamma$  line as Na  $s$  states lies below Bi  $p$  states. However, we note that the band crossing along the A- $\Gamma$  line is much flatter compared to the pure  $Na_3Bi$ , suggesting that at this concentration the system is close to reverting the band inversion.

Since IS is broken, the double degeneracy of the bands are lifted, in general. However, the anti-commutation of the symmetry operators  $M_{110}$  and  $C_3$  of this point group ensures the double degeneracy along the hexagonal axis, A- $\Gamma$ -A line  $(0,0,k_z)$  (see discussion in Sec. III A 3). Because of the maintained band inversion, the doubly degenerate valence and conduction bands cross on this line at the Fermi energy at  $(0, 0, \pm 0.083)$  ( $1/\text{\AA}$ ) forming two Dirac nodes. The topological analysis confirms that the chirality of the nodes is zero. As in the case of pure  $Na_3Bi$ , the  $Z_2$  invariant of  $k_z = 0$  plane is 1. To complete the analysis, we have calculated Fermi arc surface states as shown in the inset of Fig 12(b), which are similar to the arcs of the pure system. Therefore, our analysis shows that this system with 50% impurity is still a DSM. However, we would like to emphasize that although this phase is considered as a DSM phase because of the presence of two doubly-degenerate Dirac nodes, the dispersion around the DPs is different from that of the pure  $Na_3Bi$  for the same reason as explained in Sec. III A 3.

When both Bi atoms are replaced by Sb atoms to construct the  $Na_3Sb$  crystal, a gap opens up at the Fermi level. A trivial  $Z_2$  invariant confirms that the system is a trivial insulator. The results shown in this section are consistent with previous work done using CPA approximation[38].

We have also carried out a study of the effect of broken TRS in  $Na_3Bi$  by substituting one Bi by one Mn atom. Because of the high Mn concentration, the system simply turns into a trivial magnetic metal. To address systems with a lower concentration, it is necessary to consider considerably larger supercell than the one considered here. This in turns makes the topological analysis unwieldy due the need of considering a large number of maximally localized Wannier functions, as explained in Sec. II.

#### V. CONCLUSIONS

In this work we have used first-principles DFT methods to study the electronic, magnetic and topological properties of doped DSMs. Specifically, we have considered  $Cd_3As_2$  and  $Na_3Bi$ , two well-established DSMs, focusing in particular on the first, with the goal of investigating whether it is possible to trigger topological phase transitions by breaking selectively different symmetries, namely IS, TRS and the rotational symmetry by non-

magnetic and magnetic chemical doping.

We found that when the rotational (screw) symmetry of  $Cd_3As_2$  is broken while preserving IS, a gap opens up between the conduction and valence bands, confirming the expectation that the rotational symmetry is crucial for the stability of the Dirac points. Although the system is still a semimetal due to the presence of electron and hole pockets, the valence band is completely separated from the conduction band everywhere in the BZ (see Fig 2) and the  $Z_2$  calculation shows that the  $k_x, k_y, k_z = 0$  TRIPs are all topologically nontrivial. If both IS and rotational symmetries are broken, then each Dirac node splits into two Weyl nodes with opposite chirality i.e. the system makes a transition to Weyl phase.

The most interesting topological phase in  $Cd_3As_2$  arises when IS is broken while the rotational screw symmetry is preserved. Due to the presence of the crystal symmetries such as the mirror plane and the rotational screw axis, along with the TRS, the two-fold degeneracy of the bands is still maintained along the tetragonal axis. Therefore, the original Dirac points survive despite the broken IS. At generic points away from the tetragonal axis, double degeneracy is lifted and our calculation shows the occurrence of band crossings at eight different points in the  $k_z = 0$  plane, close to the Fermi level. The topological analysis confirmed that they form four pairs of Weyl nodes, each pair consisting of nodes with opposite chirality. Therefore, this particular realization of impurity doping results in a coexisting Dirac-Weyl phase. This numerical finding was corroborated by a continuum  $\mathbf{k} \cdot \mathbf{p}$  which allowed us to elucidate the topological nature of this phase and its stability. Although the coexisting phase was explicitly obtained for an unrelaxed configuration, we showed that in the presence of an additional external strain such a phase should emerge at the strain-induced topological phase transition point separating a trivial semimetal phase from a DSM phase. It is also possible that this mixed phase could be present in a system for a small range of external stress around this transition point.

We have also investigated the consequence of breaking TRS while preserving IS by introducing two Mn impurity. Since TRS is broken, the system cannot host any Dirac node. Instead, the system makes a transition to a magnetic WSM phase with four Weyl nodes close to the Fermi level. The topological analysis shows that the

Chern number for  $k_x = 0$  plane is 1, which signifies that this plane may be viewed as 2D Chern insulator. Therefore, this magnetically-doped DSM that transforms into WSM provides a possible platform to realize the quantum anomalous Hall effect. In the case when both IS and TRS are broken by a single Mn impurity in  $Cd_3As_2$ , it also transform into a magnetic WSM but the Weyl points reside further away from the Fermi level.

One final important remark regards the experimental realization of the different doping cases that we have analyzed in this work. We recognize that achieving the precise breaking of one particular symmetry while preserving others in a bulk system is a highly nontrivial endeavor from the experimental point of view. A more realistic treatment of doping should include some degree of disorder, which can possibly affect some of the phases considered here. However, we believe that some of the cases that we have investigated in this work, such as the one with a single impurity (both magnetic and nonmagnetic) can be realized experimentally, since for a large enough unit cell this essentially represents a random doping. We also believe that the impurity case displaying the coexisting Dirac+Weyl phase (IS broken but rotational symmetry preserved) can be realized by delta-doping  $Cd_3As_2$  with MBE techniques, forming a layered structure (Fig. 1) that should be relatively more robust against disorder by individual impurities. Therefore, we hope that our work will encourage experimental investigations of impurity-induced phase transitions in these topological semimetal materials.

## ACKNOWLEDGMENTS

We would like to thank Awadhesh Narayan for useful comments on Ref. 38. This work was supported by the Swedish Research Council (VR) through Grant No. 621-2014-4785, Grant No. 2017-04404, and by the Carl Tryggers Stiftelse through Grant No. CTS 14:178. Computational resources have been provided by the Lunarc Center for Scientific and Technical Computing at Lund University. We also acknowledge CINECA for computer resources allocated under ISCRA initiative and R. Colnaghi for technical support on computer hardware.

- 
- [1] M. Z. Hasan and C. L. Kane, Rev. Mod. Phys. **82**, 3045 (2010).
  - [2] B. Yan and S.-C. Zhang, Reports on Progress in Physics **75**, 096501 (2012).
  - [3] B. Yan and C. Felser, Annu. Rev. Condens. Matter Phys. **8**, 337 (2017).
  - [4] M. Z. Hasan, S.-Y. Xu, I. Belopolski, and S.-M. Huang, Annu. Rev. Condens. Matter Phys. **8**, 289 (2017).
  - [5] G. Chang, B. Wieder, F. Schindler, D. Sanchez, I. Belopolski, S.-M. Huang, B. Singh, D. Wu, T.-R. Chang, T. Neupert, S.-Y. Xu, H. Lin, and M. Z. Hasan, Nat. Mater. **17** (2018).
  - [6] C. L. Kane and E. J. Mele, Phys. Rev. Lett. **95**, 146802 (2005).
  - [7] B. A. Bernevig, T. L. Hughes, and S.-C. Zhang, Science **314**, 1757 (2006).

- [8] M. König, S. Wiedmann, C. Brüne, A. Roth, H. Buhmann, L. W. Molenkamp, X.-L. Qi, and S.-C. Zhang, *Science* **318**, 766 (2007).
- [9] S. Murakami, *New Journal of Physics* **9**, 356 (2007).
- [10] N. P. Armitage, E. J. Mele, and A. Vishwanath, *Rev. Mod. Phys.* **90**, 015001 (2018).
- [11] Z. Wang, Y. Sun, X.-Q. Chen, C. Franchini, G. Xu, H. Weng, X. Dai, and Z. Fang, *Phys. Rev. B* **85**, 195320 (2012).
- [12] Z. Wang, H. Weng, Q. Wu, X. Dai, and Z. Fang, *Phys. Rev. B* **88**, 125427 (2013).
- [13] S. Borisenko, Q. Gibson, D. Evtushinsky, V. Zabolotnyy, B. Büchner, and R. J. Cava, *Phys. Rev. Lett.* **113**, 027603 (2014).
- [14] Z. K. Liu, B. Zhou, Y. Zhang, Z. J. Wang, H. M. Weng, D. Prabhakaran, S.-K. Mo, Z. X. Shen, Z. Fang, X. Dai, Z. Hussain, and Y. L. Chen, *Science* **343**, 864 (2014).
- [15] M. Neupane, S.-Y. Xu, R. Sankar, N. Alidoust, G. Bian, C. Liu, I. Belopolski, T.-R. Chang, H.-T. Jeng, H. Lin, A. Bansil, F. Chou, and M. Z. Hasan, *Nat. Commun.* **5**, 3786 (2014).
- [16] Z.-K. Liu, J. Jiang, B. Zhou, Z. Wang, Y. Zhang, H.-M. Weng, D. Prabhakaran, S.-K. Mo, H. Peng, P. N. Dudin, T. K. Kim, M. Hoesch, Z. Fang, X.-F. Dai, Z. Shen, D. L. Feng, Z. Hussain, and Y. L. Chen, *Nat. Mater.* **13**, 677 (2014).
- [17] X. Wan, A. M. Turner, A. Vishwanath, and S. Y. Savrasov, *Phys. Rev. B* **83**, 205101 (2011).
- [18] S.-M. Huang, S.-Y. Xu, I. Belopolski, C.-C. Lee, G. Chang, B. Wang, N. Alidoust, G. Bian, M. Neupane, C. Zhang, S. Jia, A. Bansil, H. Lin, and M. Z. Hasan, *Nat. Commun.* **6**, 7373 (2015).
- [19] C.-C. Lee, S.-Y. Xu, S.-M. Huang, D. S. Sanchez, I. Belopolski, G. Chang, G. Bian, N. Alidoust, H. Zheng, M. Neupane, B. Wang, A. Bansil, M. Z. Hasan, and H. Lin, *Phys. Rev. B* **92**, 235104 (2015).
- [20] Y. Sun, S.-C. Wu, and B. Yan, *Phys. Rev. B* **92**, 115428 (2015).
- [21] B. Q. Lv, H. M. Weng, B. B. Fu, X. P. Wang, H. Miao, J. Ma, P. Richard, X. C. Huang, L. X. Zhao, G. F. Chen, Z. Fang, X. Dai, T. Qian, and H. Ding, *Phys. Rev. X* **5**, 031013 (2015).
- [22] S.-Y. Xu, I. Belopolski, D. S. Sanchez, C. Zhang, G. Chang, C. Guo, G. Bian, Z. Yuan, H. Lu, T.-R. Chang, P. P. Shibayev, M. L. Prokopovych, N. Alidoust, H. Zheng, C.-C. Lee, S.-M. Huang, R. Sankar, F. Chou, C.-H. Hsu, H.-T. Jeng, A. Bansil, T. Neupert, V. N. Strocov, H. Lin, S. Jia, and M. Z. Hasan, *Science Advances* **1** (2015).
- [23] S.-Y. Xu, I. Belopolski, N. Alidoust, M. Neupane, G. Bian, C. Zhang, R. Sankar, G. Chang, Z. Yuan, C.-C. Lee, S.-M. Huang, H. Zheng, J. Ma, D. S. Sanchez, B. Wang, A. Bansil, F. Chou, P. P. Shibayev, H. Lin, S. Jia, and M. Z. Hasan, *Science* **349**, 613 (2015).
- [24] N. Xu, H. Weng, B. Lv, C. Matt, J. Park, F. Bisti, V. Strocov, D. Gawryluk, E. Pomjakushina, K. Conder, N. Plumb, M. Radovic, G. AutÅ's, O. Yazyev, Z. Fang, X. Dai, T. Qian, J. Mesot, H. Ding, and M. Shi, *Nat. Commun.* **7**, 11006 (2016).
- [25] S. Wang, B.-C. Lin, A.-Q. Wang, D.-P. Yu, and Z.-M. Liao, *Advances in Physics: X* **2**, 518 (2017).
- [26] A. A. Zyuzin and A. A. Burkov, *Phys. Rev. B* **86**, 115133 (2012).
- [27] C.-X. Liu, P. Ye, and X.-L. Qi, *Phys. Rev. B* **87**, 235306 (2013).
- [28] P. Hosur and X. Qi, *Comptes Rendus Physique* **14**, 857 (2013).
- [29] S. A. Parameswaran, T. Grover, D. A. Abanin, D. A. Pesin, and A. Vishwanath, *Phys. Rev. X* **4**, 031035 (2014).
- [30] P. Hosur, *Phys. Rev. B* **86**, 195102 (2012).
- [31] T. Ojanen, *Phys. Rev. B* **87**, 245112 (2013).
- [32] A. Potter, I. Kimchi, and A. Vishwanath, *Nat. Commun.* **5**, 5161 (2014).
- [33] S.-Y. Xu, C. Liu, S. K. Kushwaha, R. Sankar, J. W. Krizan, I. Belopolski, M. Neupane, G. Bian, N. Alidoust, T.-R. Chang, H.-T. Jeng, C.-Y. Huang, W.-F. Tsai, H. Lin, P. P. Shibayev, F.-C. Chou, R. J. Cava, and M. Z. Hasan, *Science* **347**, 294 (2015).
- [34] M. Kargarian, M. Randeria, and Y.-M. Lu, *Proceedings of the National Academy of Sciences* **113**, 8648 (2016).
- [35] Y. Wu, N. H. Jo, L.-L. Wang, C. A. Schmidt, K. M. Neilson, B. Schruck, P. Swatek, A. Eaton, S. L. Bud'ko, P. C. Canfield, and A. Kaminski, *Phys. Rev. B* **99**, 161113 (2019).
- [36] B.-J. Yang and N. Nagaosa, *Nat. Commun.* **5**, 4898 (2014).
- [37] J. Cao, S. Liang, C. Zhang, Y. Liu, J. Huang, Z. Jin, Z.-G. Chen, Z. Wang, Q. Wang, J. Zhao, S. Li, X. Dai, J. Zou, Z. Xia, L. Li, and F. Xiu, *Nat. Commun.* **6** (2014).
- [38] A. Narayan, D. Di Sante, S. Picozzi, and S. Sanvito, *Phys. Rev. Lett.* **113**, 256403 (2014).
- [39] M.-X. Deng, W. Luo, R.-Q. Wang, L. Sheng, and D. Y. Xing, *Phys. Rev. B* **96**, 155141 (2017).
- [40] H. Gao, Y. Kim, J. W. F. Venderbos, C. L. Kane, E. J. Mele, A. M. Rappe, and W. Ren, *Phys. Rev. Lett.* **121**, 106404 (2018).
- [41] P. Giannozzi, S. Baroni, N. Bonini, M. Calandra, R. Car, C. Cavazzoni, D. Ceresoli, G. L. Chiarotti, M. Cococcioni, I. Dabo, A. Dal Corso, S. de Gironcoli, S. Fabris, G. Fratesi, R. Gebauer, U. Gerstmann, C. Gougoussis, A. Kokalj, M. Lazzeri, L. Martin-Samos, N. Marzari, F. Mauri, R. Mazzarello, S. Paolini, A. Pasquarello, L. Paulatto, C. Sbraccia, S. Scandolo, G. Sclauzero, A. P. Seitsonen, A. Smogunov, P. Umari, and R. M. Wentzcovitch, *J. Condens. Matter Phys.* **21**, 395502 (2009).
- [42] P. Blaha, K. Schwarz, G. K. H. Madsen, D. Kvasnicka, and J. Luitz, *WIEN2K, An Augmented Plane Wave Plus Local Orbitals Program for Calculating Crystal properties* (Vienna University of Technology, Austria, 2001).
- [43] J. P. Perdew, K. Burke, and M. Ernzerhof, *Phys. Rev. Lett.* **77**, 3865 (1996).
- [44] G. Kresse and J. Hafner, *Phys. Rev. B* **47**, 558 (1993).
- [45] G. Kresse and J. Furthmüller, *Comput. Mater. Sci.* **6**, 15 (1996).
- [46] A. Pietraszko and K. Lukaszewicz, *Acta Crystallographica Section B* **25**, 988 (1969).
- [47] S. Nishihaya, M. Uchida, Y. Nakazawa, and et al, *Sci. Adv.* **4**, 5668 (2018).
- [48] A. B. Mekhiya, L. N. Kazakov, A. A. and Oveshnikov, and et al., *J. Semicond.* **53**, 1439 (2019).
- [49] Y. Sun, Y. Meng, R. Dai, and et al., *Opt. Lett.* **44**, 4103 (2019).
- [50] A. A. Mostofi, J. R. Yates, G. Pizzi, Y.-S. Lee, I. Souza, D. Vanderbilt, and N. Marzari, *Comput. Phys. Commun.* **185**, 2309 (2014).

- [51] I. Souza, N. Marzari, and D. Vanderbilt, *Phys. Rev. B* **65**, 035109 (2001).
- [52] Q. Wu, S. Zhang, H.-F. Song, M. Troyer, and A. A. Soluyanov, *Comput. Phys. Commun.* **224**, 405 (2018).
- [53] A. A. Soluyanov and D. Vanderbilt, *Phys. Rev. B* **83**, 235401 (2011).
- [54] T. Zhou, C. Zhang, H. Zhang, F. Xiu, and Z. Yang, *Inorg. Chem. Front.* **3**, 1637 (2016).
- [55] A. Mosca Conte, O. Pulci, and F. Bechstedt, *Scientific Reports* **7**, 45500 (2017).
- [56] I. Crassee, R. Sankar, W.-L. Lee, A. Akrap, and M. Orlita, *Phys. Rev. Materials* **2**, 120302 (2018).
- [57] Y. Sun, Y. Zhang, C. Felser, and B. Yan, *Phys. Rev. Lett.* **117**, 146403 (2016).
- [58] Z. Wang, H. Weng, Q. Wu, X. Dai, and Z. Fang, *Physical Review B* **88** (2013).
- [59] H. Jin, Y. Dai, Y.-D. Ma, X.-R. Li, W. Wei, L. Yu, and B.-B. Huang, *J. Mater. Chem. C* **3**, 3547 (2015).